

Orbital Kerr effect and terahertz detection via the nonlinear Hall effect

Diego García Ovalle,^{*} Armando Pezo,[†] and Aurélien Manchon[‡]

Aix-Marseille Université, CNRS, CINaM, Marseille, France

(Dated: November 21, 2023)

We investigate the optical response induced by a d.c. current flowing in a nonmagnetic material that lacks inversion symmetry. In this class of materials, the flowing current experiences a nonlinear Hall effect and induces a nonequilibrium orbital magnetization, even in the absence of spin-orbit coupling. As a result, an orbital-driven Kerr effect arises that can be used to probe not only the orbital magnetization, but also the nonlinear Hall effect. In addition, in the long wavelength limit, the nonlinear Hall effect leads to a rectification current that can be used to detect terahertz radiation. We apply the theory to selected model systems, such as WTe₂ bilayer, as well as to realistic materials, i.e., bulk Te and metallic superlattices. The nonequilibrium orbital Kerr efficiencies obtained in these systems are comparable to the largest values reported experimentally in GaAs and MoS₂, exceeding the values reported in metals and suggesting a large terahertz current responsivity.

I. INTRODUCTION

Nonreciprocal transport in noncentrosymmetric quantum materials has been attracting increasing interest over the past decade [1], emphasizing the connection between nonlinear optical and electrical responses and the geometry of the Bloch states [2–4]. Among these phenomena, the nonlinear Hall effect associated with the Berry curvature dipole [5] (BCD) is particularly intriguing as it enables the generation of transverse currents even in the absence of magnetic field [6, 7]. In a recent proposal, Zhang and Fu [8] suggested that the rectification induced by the nonlinear Hall effect could be used to detect terahertz radiations, a topic gaining increasing momentum [9]. As discussed in detail below, the nonlinear Hall effect, at the second order in the electric field, is a companion of the nonequilibrium orbital magnetization [10]. Indeed, both effects only require inversion symmetry breaking and can emerge in the absence of spin-orbit coupling. Therefore, the nonlinear Hall effect is not only a signature of the BCD but also a signature of the nonequilibrium orbital magnetization. This connection is remarkably instrumental as it enables the optical probe of the nonequilibrium orbital moment via the so-called orbital-driven Kerr effect, as illustrated in Fig. 1.

In recent years, it has been proposed that orbital currents and densities can be electrically induced in noncentrosymmetric metals via the so-called orbital Hall effect [11–13] and orbital Rashba-Edelstein effect [14, 15], respectively, not necessitating spin-orbit coupling. This prediction opens wide perspectives for materials research and device development as entire families of metallic compounds made of light elements, often cheap and abundant, could in principle host interconversion phenomena between charge and orbital currents [13, 16–18]. The central role of orbital currents in spin torque [19–23], spin

pumping [24] and magnetoresistance experiments [25] has been clearly demonstrated recently.

In all the experiments mentioned above, the clear distinction between spin and orbital transport phenomena remains challenging as both classes of effects are intermingled via spin-orbit coupling. Since the orbital accumulation of conduction electrons produces a nonequilibrium orbital magnetization, it can be detected by converting this orbital signal into a chemical potential using a proximate magnetic layer for instance. This technique is typically used to detect spin accumulation in magnetic bilayers [26] or in nonlocal geometries [27]. When it comes to detecting the orbital accumulation though, a difficulty arises. Indeed, assuming that this proximate ferromagnet is made out of transition metals, its magnetization mostly comes from the spin angular momentum because of orbital quenching [28, 29]. Therefore, one needs to first convert the orbital signal into a spin signal, typically via spin-orbit coupling, as achieved in Ref. [25]. In other words, the electrical detection of nonequilibrium orbital magnetization using a bilayer configuration requires the coexistence of spin-orbit coupling and magnetism. As a result, it is virtually impossible to selectively probe the orbital accumulation using electrical means only.

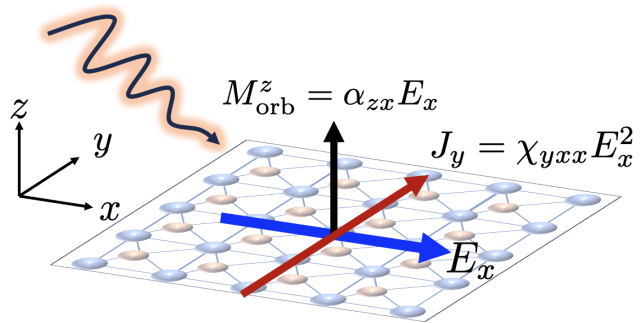


FIG. 1. (Color online) Schematics of the connection between the nonequilibrium orbital Kerr effect and the second-order anomalous Hall effect in a noncentrosymmetric, nonmagnetic metal.

^{*} diego-fernando.garcia-ovalle@univ-amu.fr

[†] armando-arquimedes.pezo-lopez@univ-amu.fr

[‡] aurelien.manchon@univ-amu.fr

An alternative method consists of using optical methods [10, 30, 31] to directly probe the orbital accumulation without relying on any magnetic material or nonlocality. Indeed, the magneto-optical Kerr (and Faraday) effect is routinely used to probe the magnetization of ferro- and ferrimagnets and image magnetic domains [32]. In this process, the spin-orbit coupling enables the generation of the spin accumulation itself as well as its coupling with the circularly polarized light. This method has been successfully used in the past to detect the current-driven spin accumulation generated via spin Hall effect in GaAs [33], Pt and W thin films [34] and Bi₂O₃ surface [35]. In light metals though, both the generation of orbital accumulation out of equilibrium and its coupling with light occur in the absence of spin-orbit coupling, which results, in principle, in a much larger nonequilibrium Kerr signal [30, 31].

In this Article, we show that the Kerr effect can be used to probe this nonequilibrium orbital magnetization, via the nonlinear anomalous Hall effect [5]. In ferromagnets, the magneto-optical Kerr effect does not directly probe the magnetization itself, but it rather probes the anomalous Hall effect of the magnetic material, so that the Kerr angle is directly related to the anomalous Hall conductivity $\theta_k + i\phi_k \sim \sigma_{xy}/\sigma_{xx}$. Hence, the mere presence of the nonlinear Hall effect guarantees the current-induced orbital-driven Kerr effect. In addition, the rectified Hall current can be used to detect the presence of low-energy photons [8], typically in the terahertz range (10 THz=12 meV). Remarkably, the "current responsivity", i.e., the performance criterion for terahertz detection, is directly proportional to the orbital Kerr efficiency in the low-frequency limit, $R \propto \theta_k$. This relation opens appealing perspectives in the search for optimal materials for terahertz detection.

Our manuscript is organized as follows: In Section II we present the general theory of the nonequilibrium orbital Kerr effect in nonmagnetic, noncentrosymmetric crystals, and establish the connection between the nonequilibrium orbital magnetization and the nonlinear Hall effect. Then, in Section III we demonstrate the proof-of-principle on bilayer WTe₂ [36] and Nb_{2n+1}Si_nTe_{4n+2} [37]. In Section IV, we present first-principles calculations on bulk Te and on a multilayer made out of transition metals. Finally, in Section V we provide a general discussion and draw the main conclusions.

II. GENERAL THEORY

A. Nonlinear magneto-optics

Without loss of generality, let us consider the magneto-optical Kerr effect in its polar version [32, 38]. Under the application of a perpendicularly incident light $\mathbf{E}_{ac} = \mathcal{E}_0 e^{i(\mathbf{k}\cdot\mathbf{z} - \omega t)}$ with frequency ω and circular polarization, the Kerr rotation angle θ_k and the ellipticity ϕ_k

can be approximated in terms of the longitudinal (σ_{xx}) and transverse (σ_{xy}) optical conductivity [38],

$$\theta_k + i\phi_k = \frac{\sigma_{xy}}{\sigma_{xx} \left(1 + \frac{4\pi i}{\omega} \sigma_{xx}\right)^{\frac{1}{2}}}. \quad (1)$$

The longitudinal conductivity in Eq. (1) can be accounted for through the Green function formula [39]

$$\sigma_{xx} = \frac{e^2}{4\pi\hbar} \int d\epsilon \partial_\epsilon f(\epsilon) \text{Re} \left\{ \text{Tr} [v_x G^{R-A} v_x G^{R-A}] \right\}, \quad (2)$$

where $G^{R(A)} = [(\epsilon + \hbar\omega) - \mathcal{H}_{\mathbf{k}} \pm i\Gamma]^{-1}$, $G^{R-A} = G^R - G^A$ and Γ is a disorder broadening. Besides, the transverse optical conductivity is given by [40]

$$\sigma_{xy} = \frac{e^2}{\hbar} \int_{BZ} \frac{d^2\mathbf{k}}{(2\pi)^2} \sum_{nm} \Omega_{nm\mathbf{k}}^z (f_{n\mathbf{k}}^{(0)} - f_{m\mathbf{k}}^{(0)}), \quad (3)$$

where $\Omega_{n\mathbf{k}}$ is the Berry curvature (BC)

$$\begin{aligned} \Omega_{n\mathbf{k}}(\omega) &= i \sum_{m \neq n} \frac{\langle u_{n\mathbf{k}} | \hat{v}_{\mathbf{k}} | u_{m\mathbf{k}} \rangle \times \langle u_{m\mathbf{k}} | \hat{v}_{\mathbf{k}} | u_{n\mathbf{k}} \rangle}{(\epsilon_{n\mathbf{k}} - \epsilon_{m\mathbf{k}})^2 - (\hbar\omega + i\Gamma)^2} \\ &= \sum_{m \neq n} \Omega_{nm\mathbf{k}} \end{aligned} \quad (4)$$

in the Bloch eigenbasis, where $\hat{v}_{\mathbf{k}} = \frac{\partial \mathcal{H}_{\mathbf{k}}}{\partial \mathbf{k}}$. Notice that in the limit $\hbar\omega \rightarrow 0$, Eq. (3) converges to the d.c. Hall conductivity [41]. In the present work, the Fermi distribution $f_{n\mathbf{k}}^{(0)}$ is taken at zero temperature such that $f_{n\mathbf{k}}^{(0)} \rightarrow -\Theta(\epsilon_{n\mathbf{k}} - \mu)$, where $\Theta(x)$ is the Heaviside step function and μ the chemical potential. From Eq. (3), it is clear that if the system is time-reversal symmetric then $\sigma_{xy} \rightarrow 0$, and thus the magneto-optical Kerr effect completely vanishes in the absence of flowing current. Notwithstanding, when time reversal is preserved and inversion symmetry is absent, a nonequilibrium Kerr effect is allowed by symmetry, revealing the underlying generation of a nonequilibrium magnetization in the process. Now, let us suppose that an additional d.c. electric field \mathbf{E}_0 is applied in the sample. Following the rationale developed by Sodemann and Fu [5] for the nonlinear Hall effect, and Yoda and Murakami [15] for the nonequilibrium orbital magnetization, the nonequilibrium Fermi distribution function reads $f_{n\mathbf{k}} = f_{n\mathbf{k}}^{(0)} + f_{n\mathbf{k}}^{(1)}$, and within the relaxation time approximation,

$$f_{n\mathbf{k}}^{(1)} = \frac{e\tau}{\hbar} \mathbf{E}_0 \cdot \partial_{\mathbf{k}} f_{n\mathbf{k}}^{(0)}, \quad (5)$$

where τ is a constant scattering time. Replacing Eq. (5) into Eq. (3), we deduce that [42]

$$\sigma_{xy} = \frac{e^3 \tau \mathbf{E}_0}{\hbar^2} \int_{BZ} \frac{d^2\mathbf{k}}{(2\pi)^2} \sum_{nm} \Omega_{nm\mathbf{k}}^z(\omega) (\partial_{\mathbf{k}} f_{n\mathbf{k}}^{(0)} - \partial_{\mathbf{k}} f_{m\mathbf{k}}^{(0)}). \quad (6)$$

Therefore, the combination of Eqs. (6) and (1) indicates that the nonequilibrium Kerr effect is proportional

to an a.c. BCD [5] [the integral in Eq. (6)], which in fact is the leading order contribution to the second-order optical conductivity at small frequencies [43]. As such, the nonequilibrium orbital magnetization, nonlinear Hall current, and nonequilibrium Kerr effect are companion phenomena in noncentrosymmetric nonmagnetic materials and heterostructures. Because of this intimate relationship between the orbital moment and the Kerr effect, we tag the latter "orbital Kerr effect". As complementary evidence of this connection, in the next section we demonstrate a general decomposition of the nonequilibrium orbital magnetization in terms of the BCD in the d.c. limit $\hbar\omega \rightarrow 0$.

Before closing this section, let us comment on the rectification effect associated with the nonlinear Hall response. As pointed out in Ref. [8], a high-frequency electric field $\mathbf{E}_{ac} = \mathbf{E}_0 \cos(\omega t)$ induces an oscillatory nonlinear Hall current [5]

$$j_i = \epsilon_{ibk} \frac{e^3 \tau}{\hbar^2} D_{jk} E_b E_j \cos^2(\omega t), \quad (7)$$

where D_{jk} is the BCD coefficient [see Eq. (12)]. The d.c. rectified Hall current $j_i^r = \langle j_i(t) \rangle$ averaged over a cycle period can be used to detect the incoming radiation. Following Ref. [8], the performance indicator of this detector is called the current responsivity R and is given by the ratio between the Hall current I_H and the absorbed power P ,

$$Rw = \frac{I_H}{P} = \frac{j^r}{\sigma_{xx} E_0^2} = \frac{\theta_k}{2E_0}, \quad (8)$$

where w is the width of the rectifier. Remarkably, the current responsivity is simply equal to half of the orbital Kerr electrical efficiency.

B. Decomposition of the nonequilibrium orbital magnetization

Let us start with the definition of the nonequilibrium orbital magnetization in the limit $\hbar\omega \rightarrow 0$, which is based on the orbital moment within the unit cell [44],

$$\mathbf{m}_{n\mathbf{k}} = i \sum_{m \neq n} \frac{\langle u_{n\mathbf{k}} | \hat{v}_{\mathbf{k}} | u_{m\mathbf{k}} \rangle \times \langle u_{m\mathbf{k}} | \hat{v}_{\mathbf{k}} | u_{n\mathbf{k}} \rangle}{(\epsilon_{n\mathbf{k}} - \epsilon_{m\mathbf{k}})}. \quad (9)$$

Since it shares the same symmetries as the Berry curvature, the equilibrium orbital magnetization is zero in nonmagnetic materials. Nevertheless, a *nonequilibrium* orbital magnetization $\mathbf{M}_{orb} = \left(\frac{e^2 \tau}{2\hbar^2}\right) \alpha \mathbf{E}$ is allowed in systems without inversion symmetry. The orbital Edelstein coefficients are defined [15, 45]

$$\alpha_{ij}(\mu) = \int_{BZ} \frac{d^2 k}{(2\pi)^2} \sum_n m_{n\mathbf{k}}^i v_{n\mathbf{k}}^j \partial_{\epsilon_{n\mathbf{k}}} f_{n\mathbf{k}}^{(0)}. \quad (10)$$

Using the definition of the Berry curvature in Eq. (4), Eq. (10) becomes

$$\begin{aligned} \alpha_{ij}(\mu) &= -i \int_{BZ} \frac{d^2 k}{(2\pi)^2} \sum_{m \neq n} (\epsilon_{n\mathbf{k}} - \epsilon_{m\mathbf{k}}) v_{n\mathbf{k}}^j \\ &\quad \left(\frac{\langle u_{n\mathbf{k}} | \hat{v}_{\mathbf{k}} | u_{m\mathbf{k}} \rangle \times \langle u_{m\mathbf{k}} | \hat{v}_{\mathbf{k}} | u_{n\mathbf{k}} \rangle}{(\epsilon_{n\mathbf{k}} - \epsilon_{m\mathbf{k}})^2} \right)_i \delta(\epsilon_{n\mathbf{k}} - \mu) \\ &= - \int_{BZ} \frac{d^2 k}{(2\pi)^2} \sum_n (\epsilon_{n\mathbf{k}} \Omega_{n\mathbf{k}}^i - b_{n\mathbf{k}}^i) v_{n\mathbf{k}}^j \delta(\epsilon_{n\mathbf{k}} - \mu) \\ &= \mu D_{ji}(\mu) + \mathcal{B}_{ji}(\mu). \end{aligned} \quad (11)$$

As we can see from Eq. (11), the nonequilibrium orbital magnetization can be divided into two contributions: A term linear in the chemical potential and proportional to the BCD [5]

$$D_{ji} = \int_{BZ} \frac{d^2 k}{(2\pi)^2} \left[\sum_n v_{n\mathbf{k}}^j \Omega_{n\mathbf{k}}^i \partial_{\epsilon_{n\mathbf{k}}} f_{n\mathbf{k}}^{(0)} \right], \quad (12)$$

and a term that is nonlinear in μ arising from an effective magnetic field with the same symmetries as the Berry curvature and the orbital magnetic moment,

$$\mathbf{b}_{n\mathbf{k}}(\omega) = i \sum_{m \neq n} \epsilon_{m\mathbf{k}} \frac{\langle u_{n\mathbf{k}} | \hat{v}_{\mathbf{k}} | u_{m\mathbf{k}} \rangle \times \langle u_{m\mathbf{k}} | \hat{v}_{\mathbf{k}} | u_{n\mathbf{k}} \rangle}{(\epsilon_{n\mathbf{k}} - \epsilon_{m\mathbf{k}})^2 - (\hbar\omega + i\Gamma)^2}. \quad (13)$$

Remarkably, expression (11) goes one step forward from previous studies relating Berry curvature and orbital magnetic moment in the vicinity of the gap [36] and for two-band systems with particle-hole symmetry [46].

III. TWO DIMENSIONAL NONMAGNETIC SYSTEMS

In this section, we compute the Kerr angle and analyze the previous decomposition for the current-induced orbital magnetization in the cases of WTe₂ bilayer and Nb_{2n+1}Si_nTe_{4n+2} monolayer.

A. WTe₂ bilayer

In order to illustrate our theory, we start by computing θ_k and ϕ_k in the exemplary case of the WTe₂ bilayer [36], in which strong signatures of second-order Hall effect has been reported experimentally [6, 7]. The minimal model is composed of four tilted Dirac Hamiltonians in the form [36]

$$\mathcal{H}_{\mathbf{k}} = \begin{pmatrix} \mathcal{H}_{\mathbf{k}}^{d1} & \mathcal{P}_{\mathbf{k}} & 0 & \gamma \\ \mathcal{P}_{\mathbf{k}}^\dagger & \mathcal{H}_{\mathbf{k}}^{d1} & \gamma & 0 \\ 0 & \gamma & \mathcal{H}_{\mathbf{k}}^{d2} & \mathcal{P}_{\mathbf{k}} \\ \gamma & 0 & \mathcal{P}_{\mathbf{k}}^\dagger & \mathcal{H}_{\mathbf{k}}^{d2} \end{pmatrix}, \quad (14)$$

where $\mathcal{H}_{\mathbf{k}}^{di}$ describes the tilted Dirac cone at \mathbf{K}_i ,

$$\begin{aligned} \mathcal{H}_{\mathbf{k}}^{di} = & [E_i + t_i(k_x + K_i)]\hat{\sigma}_0 \\ & + v_i[k_y\hat{\sigma}_1 + \eta_i(k_x + K_i)\hat{\sigma}_2] + \frac{m_i\hat{\sigma}_3}{2}, \end{aligned} \quad (15)$$

where $\hat{\sigma}_i$, $i = 1..3$ are the Pauli spin matrices, $\hat{\sigma}_0 = 1_{2 \times 2}$, and γ is an interlayer coupling between the layers. In addition,

$$\mathcal{P}_{\mathbf{k}} = \begin{pmatrix} \nu_x k_x - i\nu_y k_y & 0 \\ 0 & -\nu_x k_x - i\nu_y k_y \end{pmatrix} \quad (16)$$

is a matrix that contains the spin-orbit coupling strength ν_x (ν_y) along \mathbf{x} (\mathbf{y}). Since the Berry curvature of the eigenstates of Eq. (14) is highly concentrated around the Dirac cones [36], we perform our calculations in the domain $[-\pi, \pi] \times [-\pi, \pi]$ for simplicity. The Berry curvature and the nonequilibrium orbital moment are perpendicular to the (k_x, k_y) plane, and since the system also has a mirror symmetry along k_y , only D_{xz} and α_{zx} are non zero. Therefore, when the electric field is applied along \hat{x} and the Berry curvature is along \hat{z} , the resulting orbital magnetization is along \hat{z} and the Hall current flows along \hat{y} . From the symmetry perspective, we can interpret the second-order Hall current along \hat{y} as the interplay between the nonequilibrium orbital magnetization along \hat{z} and the external electric field applied along \hat{x} .

The real and imaginary parts of the a.c. BCD and the longitudinal conductivity as a function of the incoming light energy are reported in Figs. 2(a,b) and (c), respectively. In the calculation discussed below, the electric field is applied at 45° with respect to the \hat{x} axis in order to retain the polar configuration. While the real part of the BCD converges to a finite but non zero value at $\hbar\omega \rightarrow 0$, the imaginary part goes to zero at zero frequency. In addition, $\text{Re}(D)$ and $\text{Im}(D)$ are concentrated at energies $\hbar\omega \leq 250$ meV, corresponding to the model system's bandwidth. The longitudinal conductivity [Fig. 2(c)] steadily increases with $\hbar\omega$ and remains mostly independent of the spin-orbit coupling parameter ν_x . In contrast, both real and imaginary parts of the BCD are highly sensitive to spin-orbit coupling and present a sharply peaked structure. Nonetheless, there is no simple relationship between the BCD peaks and peculiarities in the band structure (avoided band crossing and Berry curvature maxima). From the BCD, one can compute the Kerr angle and ellipticity, displayed in Figs. 2(d,e), that show a similar energy dependence as the BCD: at $\nu_x = 0$, the peak around 125 meV corresponds to the maximum of $\text{Re}(D)$ and $\text{Im}(D)$ for the same energy. For $\nu_x \neq 0$, the average value of θ_k and ϕ_k becomes large by increasing the spin-orbit coupling. The high sensitivity of the nonlinear Hall effect and orbital Kerr response on spin-orbit coupling suggests that these properties can be controlled externally with a gate voltage [36].

The terahertz current responsivity, defined in Eq. (7), is readily obtained from Fig. 2(d). Contrary to what

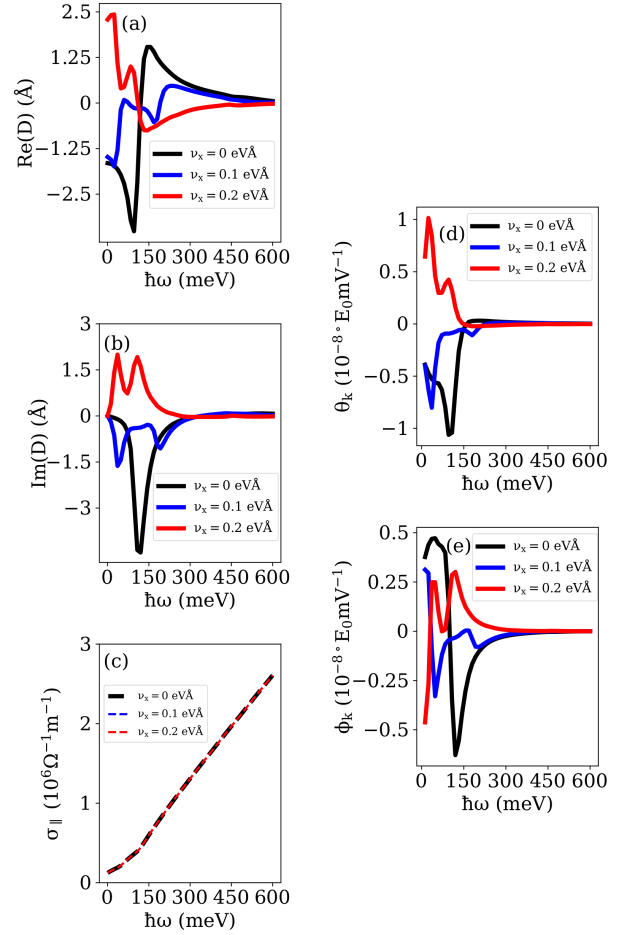


FIG. 2. (Color online) Real (a) and imaginary (b) part of the a.c. BCD as a function of the energy of the incident light for different values of spin-orbit coupling ν_x and taking $\mu = 0$. (c) Corresponding longitudinal conductivity, (d) Kerr rotation, and (e) ellipticity. We consider the values adopted in Ref. [36]: $\nu_y = 0$, $\gamma = 0.05$ eV, $K_1 = 0.1\pi \text{ \AA}^{-1}$, $K_2 = 0.15\pi \text{ \AA}^{-1}$, $v_1 = v_2 = 2$ eVÅ, $t_1 = t_2 = 1.5$ eV Å, $m_1 = m_2 = 0.1$ eV, $\eta_1 = -\eta_2 = -1$, $E_1 = 0.02$ eV, $E_2 = -0.08$ eV and $\Gamma = 0.01$ eV.

was claimed in Ref. [8], the responsivity is frequency-dependent, which means that it can be optimized through band structure engineering. The current responsivity obtained at 50 meV ($\equiv 12 \text{ THz} \equiv 3.3 \text{ mm}$) is about 10^{-2} ($\text{A} \cdot \mu\text{m}$)/W, midway between GeTe and NbP [8].

As an additional probe of the connection between the nonequilibrium orbital magnetization and the second-order Hall effect, in the d.c. limit $\hbar\omega \rightarrow 0$, we evaluate the decomposition of the orbital magnetization given by Eq. (11). In fact, such a relationship has been proposed by Son et al. [10] in the vicinity of the gap of strained MoS₂, and we intend to assess the validity of this connection in the more complex case of WTe₂ bilayer. As explained above, the low-energy Hamiltonian of WTe₂ couples four tilted Dirac cones defined as

$h_0 = E_i + t_i(k_x + K_i)$. The term $E_i + t_i K_i$ results in a rigid energy shift and $t_i k_x$ is an odd function in k_x . Consequently, we expect that the first term in Eq. (11) must dominate over \mathcal{B} close to the neutrality point. In other words, the orbital Edelstein effect in WTe₂ bilayer must follow $\alpha_{zx} \simeq \mu D_{zx}$, as long as the chemical potential μ remains in the vicinity of the Dirac nodes. These two terms, α_{zx} and μD_{zx} , are reported in Fig. 3 as a function of μ for different values of the spin-orbit coupling. When $\nu_x = 0$ [Fig. 3(a)], the system possesses two tilted Dirac cones and $\alpha_{zx} \simeq \mu D_{zx}$. Upon increasing the spin-orbit coupling [Figs. 3(b,c)], the system exhibits band inversion and anticrossing (see Ref. [36]) such that the linear relationship between the nonlinear Hall effect and nonequilibrium orbital moment fails due to discontinuity in the Berry curvature related to topological transitions. At $\nu_x = 0.4$ eV Å [Fig. 3(d)], a gap opens and the linear relation between α_{zx} and D_{zx} is restored. In other words, the validity of the phenomenological relationship between the BCD and the orbital Edelstein effect claimed in Ref. [10] is not universal and only holds as long as the band structure can be approximated by a gapped Dirac cone (as in MoS₂ and numerous transition metal dichalcogenides).

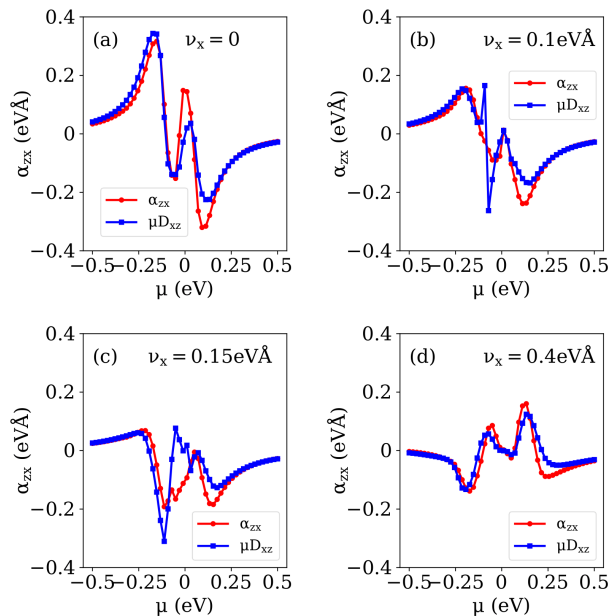


FIG. 3. (Color online) Comparison between the orbital Edelstein coefficients and the BCD for the minimal model of WTe₂ bilayer, for different values of ν_x and as a function of μ . We fix the same microscopic parameters that in Fig. 2, exemplifying the cases (a) $\nu_x = 0$, (b) $\nu_x = 0.1$ eV Å, (c) $\nu_x = 0.15$ eV Å and (d) $\nu_x = 0.4$ eV Å.

B. Nb_{2n+1}Si_nTe_{4n+2} monolayer

Large nonlinear Hall effect and orbital Kerr effect are expected to be found in materials displaying diverging Berry curvature close to Fermi level, i.e., typically Dirac or Weyl semimetals [47]. Recently, it has been proposed that the family of van der Waals compounds Nb_{2n+1}Si_nTe_{4n+2} can also display Dirac nodes [48] and nodal lines [49]. A model Hamiltonian for such a system reads $\mathcal{H}_{\mathbf{k}} = \mathcal{H}_{\mathbf{k}}^{(0)} + \mathcal{H}_{\mathbf{k}}^{(soc)}$, where [37]

$$\begin{aligned} \mathcal{H}_{\mathbf{k}}^{(0)} = & t \begin{pmatrix} 0 & 1 + e^{-ik_x} \\ 1 + e^{ik_x} & 0 \end{pmatrix} \otimes \hat{\sigma}_0 \\ & + \delta t \begin{pmatrix} 0 & e^{-ik_y}(1 + e^{-ik_x}) \\ e^{ik_y}(1 + e^{ik_x}) & 0 \end{pmatrix} \otimes \hat{\sigma}_0, \end{aligned} \quad (17)$$

$$\begin{aligned} \mathcal{H}_{\mathbf{k}}^{(soc)} = & t \begin{pmatrix} \lambda_1 \sin k_x & 0 \\ 0 & -2\lambda_1 \sin k_x \end{pmatrix} \otimes \hat{\sigma}_3 + \\ & + \delta t \begin{pmatrix} 2\lambda_3 \sin k_y & i\lambda_2 e^{ik_y}(1 + e^{-ik_x}) \\ -i\lambda_2 e^{-ik_y}(1 + e^{ik_x}) & 2\lambda_3 \sin k_y \end{pmatrix} \otimes \hat{\sigma}_3. \end{aligned} \quad (18)$$

In Eqs. (17)-(18), t and δt are the intra and inter-chain hopping parameters, respectively, and λ_i ($i = 1 \dots 3$) are the Rashba parameters. Considering that the Berry curvature and the orbital moment are parallel to \hat{z} , the nonequilibrium orbital magnetization is along \hat{z} and a current flowing along \hat{y} generates a second-order Hall current along \hat{x} with the BCD coefficient D_{yz} . Let us first study the nonequilibrium orbital Kerr effect in this system, showing the behavior of the BCD, the longitudinal conductivity, and the Kerr angle as a function of the energy of the incident light. Our results are reported in Fig. 4 for the same incidence angle as for WTe₂ bilayer.

In Fig. 4(a), we verify that at zero frequency the real part of the BCD is finite while its imaginary part vanishes, as expected. The coefficients also tend to zero upon increasing the frequency, with peaks close to $\hbar\omega \rightarrow 100$ meV. Besides, the longitudinal conductivity is almost a constant for the region $\hbar\omega \leq 300$ meV [Fig. 4(b)] and then decreases slowly with the frequency. This signal has the same order of magnitude as the response reported in previous experiments on Nb₃SiTe₆ [50, 51], whereas the nonequilibrium orbital Kerr effect is comparable to the one computed in WTe₂ bilayer in the previous section. We also find that restoring inversion symmetry by tuning the inter-chain hopping to zero progressively quenches the BCD [Fig. 4(d,e)] and nonequilibrium orbital Kerr effect [Fig. 4(f)]. Finally, Fig. 5 shows the orbital Edelstein coefficient and BCD, α_{zy} and μD_{yz} , as a function of the chemical potential μ in the d.c. limit. Whereas both functions have a similar behavior, their magnitude is markedly different. This again suggests that although both the nonequilibrium orbital moment and nonlinear anomalous Hall effect are companion phenomena that exist under the same symmetry-breaking conditions, an

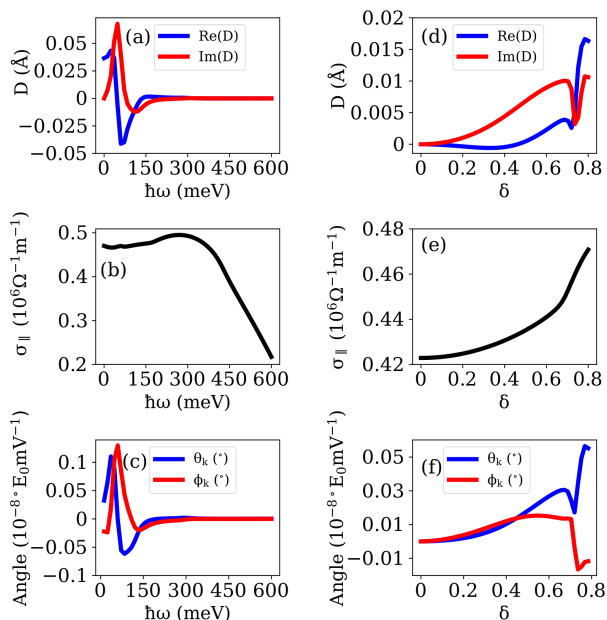


FIG. 4. (Color online) (a) Real (blue line) and imaginary (red line) part of the a.c. BCD as a function of the energy of the incident light for the Nb_{2n+1}Si_nTe_{4n+2} monolayer. (b) Longitudinal conductivity of the system, (c) Kerr angle (blue line), and ellipticity (red line) as a function of the energy of the incident light. (d,e,f) Same quantities as a function of inter-chain parameter δ . We set the parameters to $t = -0.2$ eV, $t' = \delta t = -0.16$ eV, $\lambda_1 = 1$, $\lambda_2 = \lambda_3 = 0.1$, $\mu = -0.028$ eV, $\hbar\omega = 100$ meV and $\Gamma = 0.01$ eV.

explicit relationship between these two mechanisms can only be established in the limiting case of gapped Dirac systems.

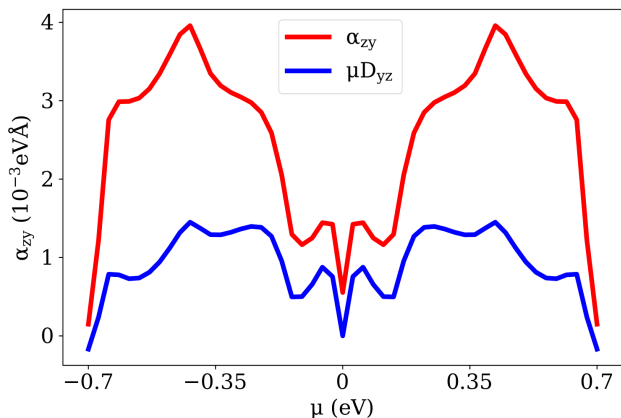


FIG. 5. (Color online) Orbital Edelstein coefficient α_{zy} and BCD coefficient μD_{yz} as a function of the chemical potential for the Nb_{2n+1}Si_nTe_{4n+2} monolayer. The microscopic parameters are $t = -0.2$ eV, $t' = \delta t = -0.16$ eV, $\lambda_1 = 1$, $\lambda_2 = \lambda_3 = 0.1$ and $\mu = -0.028$ eV.

IV. ORBITAL KERR EFFECT FROM FIRST PRINCIPLES

To illustrate the emergence of the orbital Kerr effect in a realistic system, we perform first principles simulations on two different structures lacking inversion symmetry, namely, trigonal Te and a superlattice made of an infinite repetition of W(2)/Pt(2)/V(1) trilayers. We have used a plane-wave basis set to obtain the optimized structures employing the Perdew-Burke-Ernzerhof (PBE) [52, 53] exchange-correlation functional implemented in the VASP package [54, 55]. In these simulations, we used 400 eV for the plane-wave expansion cutoff, and ionic potentials are described using the projector augmented-wave (PAW) method [56] performing the geometry optimization with a force criterion of 5×10^{-3} eV/Å. To the best of our knowledge, bulk Te is the first noncentrosymmetric material in which current-driven optical activity has been reported [57]. In Te, the combination of inversion symmetry breaking and spin-orbit coupling induces a Rashba splitting of the valence band. Therefore, injecting a current modifies the balance between carriers of opposite spin chirality, resulting in nonequilibrium circular dichroism. The W(2)/Pt(2)/V(1) metallic superlattice on the other hand is a rather conventional system that uses standard transition metals, familiar to mainstream experimental spintronics. The band structures of both systems are depicted in Fig. 6(a,b), where the Fermi level is set to zero. The unit cell structure is shown in the inset.

The BCD, the longitudinal conductivity, and the resulting nonequilibrium orbital Kerr effect are reported in Fig. 7 for both Te (left panels) and the W(2)/Pt(2)/V(1) superlattice (right panels). We emphasize that, in both systems, the inversion symmetry is broken along \hat{z} , which means that the orbital Edelstein effect generates a nonequilibrium orbital moment in the plane perpendicular to \hat{z} . Therefore, applying a current in the (x, y) plane generates a second-order Hall current along \hat{z} . To measure the second-order Hall current experimentally in the W(2)/Pt(2)/V(1) superlattice, one needs to probe the current that flows *perpendicular* to the plane of the stack, which is a rather unusual configuration.

Let us now consider the nonlinear Hall and orbital Kerr effect responses of Te, as displayed in Fig. 7(a-c). At low photon energy, the BCD of bulk Te is about 5×10^{-1} whereas that of the W(2)/Pt(2)/V(1) superlattice is about 5×10^{-2} . This needs to be compared with the (3D) BCD of WTe₂ bilayer [Fig. 2], $D_{3D} = D_{2D}/t = 10^{-1}$, where $t = 14$ Å is the thickness of the WTe₂ bilayer. Tellurium being a semiconductor, its a.c. conductivity increases steadily upon increasing the photon energy below 1 eV. As a result, the orbital Kerr effect is rather large at low photon energy, displaying a Kerr angle about three orders of magnitude larger than for the WTe₂ bilayer. On the other hand, in the W(2)/Pt(2)/V(1) superlattice [Fig. 7(d-f)], both the BCD and the orbital Kerr effect are substantially reduced, which results in a Kerr angle

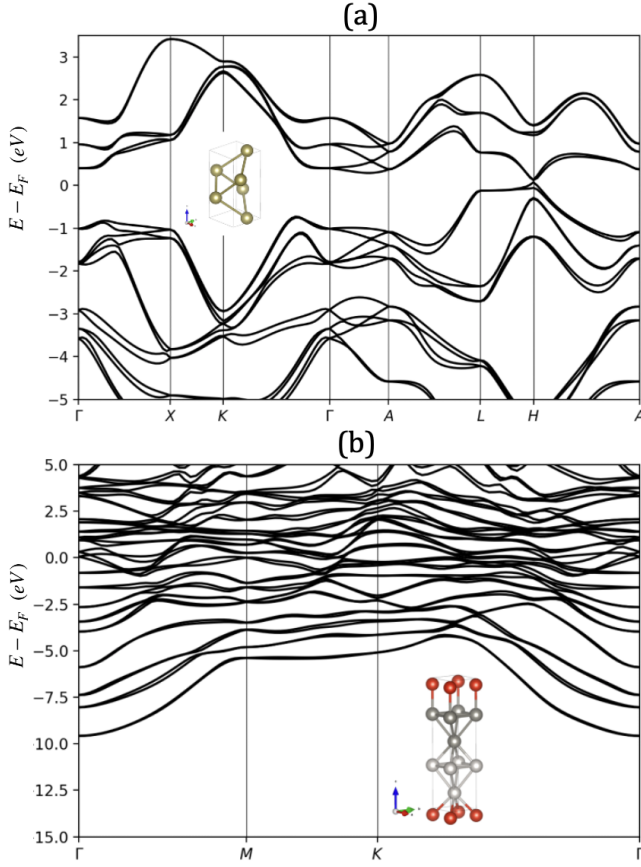


FIG. 6. (Color online) Electronic band structure of (a) trigonal Te and (b) W(2)/Pt(2)/V(1) superlattice stacked along (110). The unit cells are depicted in the inset.

about two orders of magnitude lower than in WTe₂.

Noticeably, the terahertz current responsivity of bulk Tellurium is particularly large, reaching about $Rw \approx 15$ (A $\cdot\mu\text{m}$)/W because of its low conductivity at low frequency. This value, consistent with earlier experiments [57], is comparable to NbP [8] and among the best current responsivities reported so far [58, 59].

To complete this study, the orbital Edelstein coefficients of bulk Te and W(2)/Pt(2)/V(1) superlattice are displayed in Fig. 8 as a function of the carrier energy. Again, to compare with the value computed in WTe₂ bilayer, one needs to divide the orbital Rashba coefficient of WTe₂ bilayer by the thickness, giving an order of magnitude of about 10^{-3} , about one order of magnitude larger than the orbital Edelstein coefficients computed in bulk Te and W(2)/Pt(2)/V(1) superlattice. This result suggests that interfacial engineering could be a practical path to obtain large current-driven orbital magnetization and nonlinear Hall effect.

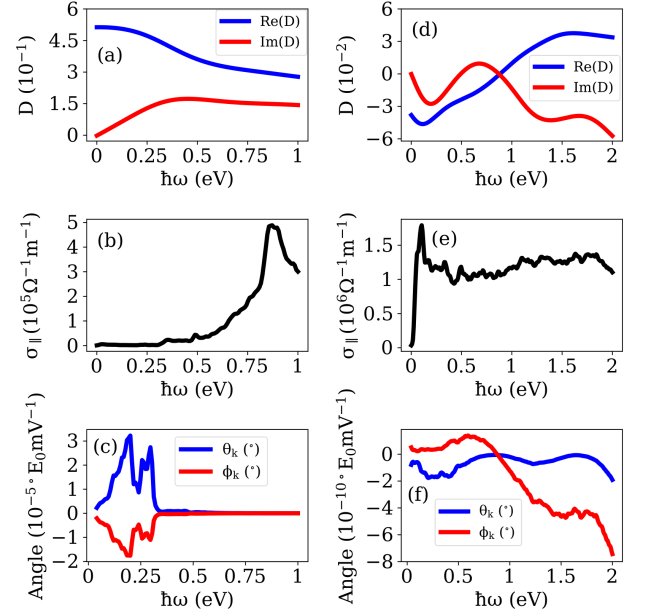


FIG. 7. (Color online) (a) Real (blue line) and imaginary (red line) part of the BCD, (b) longitudinal conductivity and (c) nonequilibrium orbital Kerr effect for bulk Te as a function of the energy of the incident light. (d) Real (blue line) and imaginary (red line) part of the BCD, (e) longitudinal conductivity, and (f) orbital Kerr effect for W(2)/Pt(2)/V(1) superlattice.

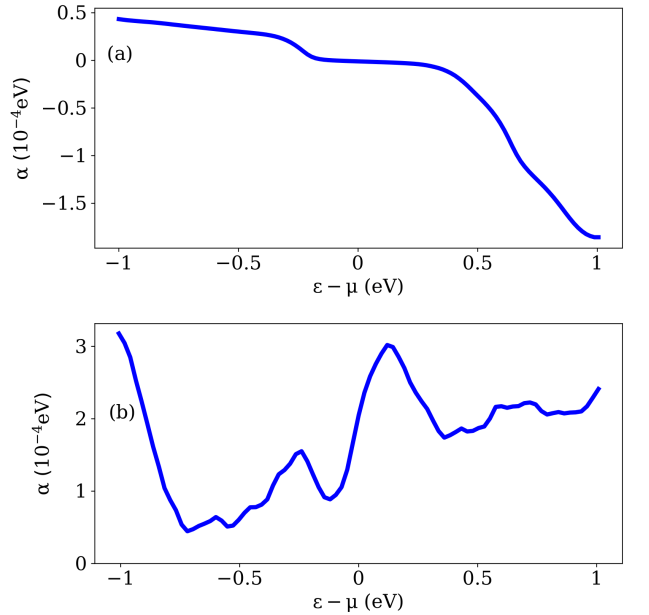


FIG. 8. (Color online) Orbital Edelstein coefficient as a function of the carrier energy for (a) bulk Te and (b) W(2)/Pt(2)/V(1) superlattice.

V. DISCUSSION AND CONCLUSION

In order to assess the ability of orbital Kerr effect to probe the nonequilibrium orbital accumulation in realistic situations, we now compare our results with experimental data obtained on different material platforms. We collected the value of the nonequilibrium orbital Kerr effect efficiencies, θ/j and θ/E_0 , for various systems published in the literature in Table I, together with representative values obtained in the present work. We stress that comparing experiments is not an easy task because the conductivity of the materials (from 10^3 to $10^7 \Omega^{-1}\cdot\text{m}^{-1}$) and the wavelength of light used for magneto-optical detection (from $10.6 \mu\text{m}$ to 514 nm) can be vastly different.

Material	λ nm	σ $\Omega^{-1}\cdot\text{m}^{-1}$	θ/j rad/(A/cm ²)	θ/E_0 rad/(V/m)	Ref.
WTe ₂	10.6×10^3	4.3×10^5	-3×10^{-12}	-1.3×10^{-10}	
NbSiTe	10.6×10^3	4.7×10^5	-1.5×10^{-13}	-7.2×10^{-12}	
W/Pt/V	10.6×10^3	1.6×10^6	-4.9×10^{-13}	-7.9×10^{-11}	
Te	10.6×10^3	1.7×10^3	8.4×10^{-5}	1.5×10^{-5}	
GaAs	825	2.8×10^3	7×10^{-10}	2×10^{-10}	[33]
MoS ₂	~ 660	10^3	8.5×10^{-11}	8.5×10^{-12}	[10]
Pt	514	6×10^6	2.3×10^{-15}	1.4×10^{-12}	[34]
Pt	800	7×10^6	3×10^{-16}	2×10^{-13}	[31]
W	514	6×10^5	-6.6×10^{-15}	-4×10^{-13}	[34]
Ti	780	2.5×10^6	-5×10^{-15}	-1.2×10^{-12}	[30]
Cr	800	5×10^6	-1.2×10^{-15}	-6×10^{-13}	[31]
Te	10.6×10^3		3.5×10^{-5}	-	[57]

TABLE I. Summary of the magneto-optical Kerr efficiencies calculated (top) and measured (bottom) in different materials. (top) In the theoretical data, we fixed the wavelength of the incident light to $\hbar\omega = 117 \text{ meV}$. (bottom) The experimental values have been extracted from the literature when available.

Let us start by considering the results obtained on GaAs in the seminal work of Kato et al. [33]. Except for Te, the electrical orbital Kerr efficiency obtained by Kato et al. is the largest reported to far, $\theta_{\text{GaAs}}/E_0 \simeq 2 \times 10^{-10} \text{ rad m V}^{-1}$, which is comparable to our numerical results for the WTe₂ bilayer and the W/Pt/V superlattice. Interestingly, this observation is interpreted in the framework of the spin Hall effect, which is rather surprising considering the very small spin-orbit coupling of GaAs. Although it would require further investigation, we speculate that this unexpectedly large value could perhaps be related to the nonequilibrium orbital accumulation rather than to spin accumulation.

When considering the ratio between the Kerr angle and the current, θ/j , we see a drastic difference between semiconductors (GaAs, MoS₂, and Te), and metallic systems (Cr, Ti, Pt, and W). The formers display an orbital Kerr efficiency that is about four orders of magnitude larger than their metallic counterpart. When considering the ratio θ/E_0 , the orbital Kerr efficiency of MoS₂ remains

one order of magnitude larger than in metals. The theoretical values computed in the present work are all larger than the values collected in metallic systems. Notice that trigonal Te stands out as the most efficient material for the orbital Kerr effect, exceeding the Kerr efficiencies of all the other materials by orders of magnitude. This intriguing observation calls for further theoretical and experimental study of this material.

The connection between the orbital Kerr effect and the current responsivity to terahertz radiation is particularly interesting. We found that the narrow-gapped semiconductor Te supports a giant current responsivity ($Rw \approx 15 \text{ (A}\cdot\mu\text{m)/W}$) whereas (semi)metallic systems like WTe₂ and W/Pt/V superlattices, that possess a relatively large BCD, display a smaller responsivity due to their high conductivity ($Rw \approx 10^{-4} \text{ (A}\cdot\mu\text{m)/W}$). This finding opens inspiring outlooks for the search for efficient terahertz rectifiers among Weyl semimetals and other topological materials with diverging Berry curvature.

In conclusion, we investigate the current-induced orbital Kerr effect and terahertz current responsivity in nonmagnetic, noncentrosymmetric materials displaying nonlinear Hall effect. In this case, the Kerr rotation is proportional to the a.c. BCD, and is therefore directly connected to the nonlinear Hall effect. The terahertz current responsivity is itself equal to half the orbital Kerr efficiency. We examined the orbital Kerr effect in selected noncentrosymmetric materials, using both effective models and realistic materials based on *ab initio* simulations, and compared our results with available experimental data, pointing out that the orbital Kerr efficiency tends to be larger in semiconductors than in metals, irrespective of the magnitude of the material's spin-orbit coupling. This opens particularly interesting promises for the observation of this effect in light compounds. In particular, our simulations on a metallic superlattice suggest that interfacial engineering can be used to optimize the nonequilibrium orbital Kerr effect, the nonlinear Hall effect, and its ability to detect terahertz radiations. Along the same line, van der Waals heterostructures [60, 61] that combine materials with very different electronic properties (e.g., semiconducting, metallic, semimetallic) could also provide an interesting platform for the study of these effects.

ACKNOWLEDGMENTS

D.G.O. and A. M. acknowledge support from the Excellence Initiative of Aix-Marseille Université - A*Midex, a French "Investissements d'Avenir" program. A.P. was supported by the ANR ORION project, grant ANR-20-CE30-0022-01 of the French Agence Nationale de la Recherche.

- [1] Y. Tokura and N. Nagaosa, Nonreciprocal responses from non-centrosymmetric quantum materials, *Nature Communications* **9**, 3740 (2018).
- [2] T. Ideue, K. Hamamoto, S. Koshikawa, M. Ezawa, S. Shimizu, Y. Kaneko, Y. Tokura, N. Nagaosa, and Y. Iwasa, Bulk rectification effect in a polar semiconductor, *Nature Physics* **13**, 578 (2017).
- [3] Y. M. Itahashi, T. Ideue, Y. Saito, S. Shimizu, T. Ouchi, T. Nojima, and Y. Iwasa, Nonreciprocal transport in gate-induced polar superconductor sr_{1-x}ba_x2, *Science Advances* **6**, eaay9120 (2020).
- [4] Y. Li, Y. Li, P. Li, B. Fang, X. Yang, Y. Wen, D. xing Zheng, C. hui Zhang, X. He, A. Manchon, Z. H. Cheng, and X. xiang Zhang, Nonreciprocal charge transport up to room temperature in bulk rashba semiconductor α -ge₂, *Nature Communications* **12**, 540 (2021).
- [5] I. Sodemann and L. Fu, Quantum nonlinear hall effect induced by berry curvature dipole in time-reversal invariant materials, *Physical Review Letters* **115**, 216806 (2015).
- [6] Q. Ma, S.-Y. Xu, H. Shen, D. MacNeill, V. Fatemi, T. rong Chang, A. M. M. Valdivia, S. Wu, Z. Du, C. han Hsu, S. Fang, Q. D. Gibson, K. Watanabe, T. Taniguchi, robert J. Cava, E. Kaxiras, H.-Z. Lu, H. Lin, L. Fu, N. Gedik, and P. Jarillo-Herrero, Observation of the nonlinear hall effect under time-reversal-symmetric conditions, *Nature* **565**, 337 (2019).
- [7] K. Kang, T. Li, E. Sohn, J. Shan, and K. F. Mak, Nonlinear anomalous hall effect in few-layer wte₂, *Nature Materials* **18**, 324 (2019).
- [8] Y. Zhang and L. Fu, Terahertz detection based on nonlinear hall effect without magnetic field, *Proceedings of the National Academy of Sciences* **118**, e2100736118 (2021).
- [9] S. S. Dhillon, M. S. Vitiello, E. H. Linfield, A. G. Davies, M. C. Hoffmann, J. Booske, C. Paoloni, M. Gensch, P. Weightman, G. P. Williams, E. Castro-Camus, D. R. S. Cumming, F. Simoens, I. Escorcia-Carranza, J. Grant, S. Lucyszyn, M. Kuwata-Gonokami, K. Konishi, M. Koch, C. A. Schmuttenmaer, T. L. Cocker, R. Huber, A. G. Markelz, Z. D. Taylor, V. P. Wallace, J. A. Zeitler, J. Sibik, T. M. Korter, B. Ellison, S. Rea, P. Goldsmith, K. B. Cooper, R. Appleby, D. Pardo, P. G. Huggard, V. Krozer, H. Shams, M. Fice, C. Renaud, A. Seeds, A. Stöhr, M. Naftaly, N. Ridler, R. Clarke, J. E. Cunningham, and M. B. Johnston, The 2017 terahertz science and technology roadmap, *Journal of Physics D: Applied Physics* **50**, 043001 (2017).
- [10] J. Son, K. H. Kim, Y. H. Ahn, H. W. Lee, and J. Lee, Strain engineering of the berry curvature dipole and valley magnetization in monolayer mos₂, *Physical Review Letters* **123**, 36806 (2019).
- [11] B. A. Bernevig, T. L. Hughes, and S. cheng Zhang, Orbitorics : The intrinsic orbital current in p-doped silicon, *Physical Review Letters* **95**, 066601 (2005).
- [12] T. Tanaka, H. Kontani, M. Naito, T. Naito, D. Hirashima, K. Yamada, and J. Inoue, Intrinsic spin hall effect and orbital hall effect in 4d and 5d transition metals, *Physical Review B* **77**, 165117 (2008).
- [13] D. Jo, D. Go, and H. woo Lee, Gigantic intrinsic orbital hall effects in weakly spin-orbit coupled metals, *Physical Review B* **98**, 214405 (2018).
- [14] D. Go, J. philipp Hanke, P. M. Buhl, F. Freimuth, G. Bihlmayer, H. woo Lee, Y. Mokrousov, and S. Blügel, Toward surface orbitronics : giant orbital magnetism from the orbital rashba effect at the surface of sp-metals, *Scientific Reports* **7**, 46742 (2017).
- [15] T. Yoda, T. Yokoyama, and S. Murakami, Orbital edelstein effect as a condensed-matter analog of solenoids, *Nano Letters* **18**, 916 (2018).
- [16] L. Salemi, M. Berritta, and P. M. Oppeneer, Quantitative comparison of electrically induced spin and orbital polarizations in heavy-metal/ 3d-metal bilayers, *Physical Review Materials* **5**, 10.1103/PhysRevMaterials.5.074407 (2021).
- [17] A. Pezo, D. G. Ovalle, and A. Manchon, Orbital hall effect in crystals: inter-atomic versus intra-atomic contributions, *Physical Review B* **106**, 104414 (2022).
- [18] L. Salemi and P. M. Oppeneer, First-principles theory of intrinsic spin and orbital hall and nerst effects in metallic monoatomic crystals, *Physical Review Materials* **6**, 095001 (2022).
- [19] S. Ding, A. Ross, D. Go, L. Baldrati, Z. Ren, F. Freimuth, S. Becker, F. Kammerbauer, J. Yang, G. Jakob, Y. Mokrousov, and M. Kläui, Harnessing orbital-to-spin conversion of interfacial orbital currents for efficient spin-orbit torques, *Physical Review Letters* **125**, 177201 (2020).
- [20] D. Lee, D. Go, H. J. Park, W. Jeong, H. W. Ko, D. Yun, D. Jo, S. Lee, G. Go, J. H. Oh, K. J. Kim, B. G. Park, B. C. Min, H. C. Koo, H. W. Lee, O. J. Lee, and K. J. Lee, Orbital torque in magnetic bilayers, *Nature Communications* **12**, 6710 (2021).
- [21] G. Sala and P. Gambardella, Giant orbital hall effect and orbital-to-spin conversion in 3d, 5d, and 4f metallic heterostructures, *Physical Review Research* **4**, 10.1103/PhysRevResearch.4.033037 (2022).
- [22] H. Hayashi, D. Jo, D. Go, T. Gao, S. Haku, Y. Mokrousov, H. W. Lee, and K. Ando, Observation of long-range orbital transport and giant orbital torque, *Communications Physics* **6**, 10.1038/s42005-023-01139-7 (2023).
- [23] R. Fukunaga, S. Haku, H. Hayashi, and K. Ando, Orbital torque originating from orbital hall effect in zr, *Physical Review Research* **5**, 10.1103/PhysRevResearch.5.023054 (2023).
- [24] A. E. Hamdi, J. Y. Chauleau, M. Boselli, C. Thibault, C. Gorini, A. Smogunov, C. Barreteau, S. Gariglio, J. M. Triscone, and M. Viret, Observation of the orbital inverse rashba-edelstein effect, *Nature Physics* **10.1038/s41567-023-02121-4** (2023).
- [25] S. Ding, Z. Liang, D. Go, C. Yun, M. Xue, Z. Liu, S. Becker, W. Yang, H. Du, C. Wang, Y. Yang, G. Jakob, M. Kläui, Y. Mokrousov, and J. Yang, Observation of the orbital rashba-edelstein magnetoresistance, *Physical Review Letters* **128**, 067201 (2022).
- [26] H. Nakayama, M. Althammer, Y.-T. Chen, K. Uchida, Y. Kajiwara, D. Kikuchi, T. Ohtani, S. Geprägs, M. Opel, S. Takahashi, R. Gross, G. E. W. Bauer, S. T. B. Goennenwein, and E. Saitoh, Spin hall magnetoresistance induced by a nonequilibrium proximity effect, *Physical Review Letters* **110**, 206601 (2013).
- [27] S. O. Valenzuela and M. Tinkham, Direct electronic mea-

- surement of the spin hall effect., *Nature* **442**, 176 (2006).
- [28] S. Blügel and G. Bihlmayer, Magnetism of low-dimensional systems : Theory (John Wiley & Sons, 2007) pp. 1–42.
- [29] J. Hanke, F. Freimuth, A. K. Nandy, H. Zhang, S. Bl, Y. Mokrousov, and P. Gr, Role of berry phase theory for describing orbital magnetism : From magnetic heterostructures to topological orbital ferromagnets, *Physical Review B* **94**, 121114(R) (2016).
- [30] Y.-G. Choi, D. Jo, K.-H. Ko, D. Go, K.-H. Kim, H. G. Park, C. Kim, B.-C. Min, G.-M. Choi, and H.-W. Lee, Observation of the orbital hall effect in a light metal ti, *Nature* **619**, 52 (2023).
- [31] I. Lyalin, S. Alikhah, M. Berritta, P. M. Oppeneer, and R. K. Kawakami, Magneto-optical detection of the orbital hall effect in chromium, *Phys. Rev. Lett.* **131**, 156702 (2023).
- [32] J. McCord, Progress in magnetic domain observation by advanced magneto-optical microscopy, *Journal of Physics D: Applied Physics* **48**, 10.1088/0022-3727/48/33/333001 (2015).
- [33] Y. K. Kato, R. C. Myers, A. C. Gossard, and D. D. Awschalom, Observation of the spin hall effect in semiconductor., *Science (New York, N.Y.)* **306**, 1910 (2004).
- [34] C. Stamm, C. Murer, M. Berritta, J. Feng, M. Gabureac, P. M. Oppeneer, and P. Gambardella, Magneto-optical detection of the spin hall effect in pt and w thin films, *Physical Review Letters* **119**, 087203 (2017).
- [35] J. Puebla, F. Auvray, M. Xu, B. Rana, A. Albouy, H. Tsai, K. Kondou, G. Tatara, and Y. Otani, Direct optical observation of spin accumulation at nonmagnetic metal/oxide interface, *Applied Physics Letters* **111**, 10.1063/1.4990113 (2017).
- [36] Z. Z. Du, C. M. Wang, H. Z. Lu, and X. C. Xie, Band signatures for strong nonlinear hall effect in bilayer wte2, *Physical Review Letters* **121**, 10.1103/PhysRevLett.121.266601 (2018).
- [37] Y. Zhao, J. Cao, Z. Zhang, S. Li, Y. Li, F. Ma, and S. A. Yang, Berry curvature dipole and nonlinear hall effect in two-dimensional $\text{nb}_{2n+1}\text{si}_n\text{te}_{4n+2}$ 10.1103/PhysRevB.107.205124 (2023).
- [38] P. M. Oppeneer, Theory of the magneto-optical kerr effect in ferromagnetic compounds, (1999).
- [39] B. Varga and A. Manchon, Symmetrized decomposition of the kubo-bastin formula, *Physical Review B* **102**, 085113 (2020).
- [40] Y. Yao, L. Kleinman, A. H. MacDonald, J. Sinova, T. Jungwirth, D. sheng Wang, E. Wang, and Q. Niu, First principles calculation of anomalous hall conductivity in ferromagnetic bcc fe, *Physical Review Letters* **92**, 037204 (2004).
- [41] N. Nagaosa, J. Sinova, S. Onoda, A. H. MacDonald, and N. P. Ong, Anomalous hall effect, *Review of Modern Physics* **82**, 1539 (2010).
- [42] E. J. König, M. Dzero, A. Levchenko, and D. A. Pesin, Gyrotropic hall effect in berry-curved materials, *Physical Review B* **99**, 10.1103/PhysRevB.99.155404 (2019).
- [43] T. Morimoto, S. Zhong, J. Orenstein, and J. E. Moore, Semiclassical theory of nonlinear magneto-optical responses with applications to topological dirac/weyl semimetals, *Physical Review B* **94**, 10.1103/PhysRevB.94.245121 (2016).
- [44] J. Shi, G. Vignale, D. Xiao, and Q. Niu, Quantum theory of orbital magnetization and its generalization to interacting systems, *Physical Review Letters* **99**, 197202 (2007).
- [45] T. Yoda, T. Yokoyama, and S. Murakami, Current-induced orbital and spin magnetizations in crystals with helical structure, *Nature Publishing Group* , 1 (2015).
- [46] J. Xiao, A. Zangwill, and M. D. Stiles, A numerical method to solve the boltzmann equation for a spin valve, *The European Physical Journal B* **59**, 415 (2007).
- [47] N. P. Armitage, E. J. Mele, and A. Vishwanath, Weyl and dirac semimetals in three-dimensional solids, *Reviews of Modern Physics* **90**, 015001 (2018).
- [48] T. Y. Yang, Q. Wan, D. Y. Yan, Z. Zhu, Z. W. Wang, C. Peng, Y. B. Huang, R. Yu, J. Hu, Z. Q. Mao, S. Li, S. A. Yang, H. Zheng, J. F. Jia, Y. G. Shi, and N. Xu, Directional massless dirac fermions in a layered van der waals material with one-dimensional long-range order, *Nature Materials* **19**, 27 (2020).
- [49] R. Y. Liu, A. Huang, R. Sankar, J. A. Hlevyack, C. C. Su, S. C. Weng, M. K. Lin, P. Chen, C. M. Cheng, J. D. Denlinger, S. K. Mo, A. V. Fedorov, C. S. Chang, H. T. Jeng, T. M. Chuang, and T. C. Chiang, Dirac nodal line in hourglass semimetal nb3site6, *Nano Letters* **23**, 380 (2023).
- [50] J. Hu, X. Liu, C. L. Yue, J. Y. Liu, H. W. Zhu, J. B. He, J. Wei, Z. Q. Mao, L. Y. Antipina, Z. Popov, P. B. Sorokin, T. J. Liu, P. W. Adams, S. M. A. Radmanesh, L. Spinu, H. Ji, and D. Natelson, Enhanced electron coherence in atomically thin nb3site6, *Nature Physics* **11**, 471 (2015).
- [51] J. Ebad-Allah, A. A. Tsirlin, Y. L. Zhu, Z. Q. Mao, and C. A. Kuntscher, Signatures of van hove singularities in the anisotropic in-plane optical conductivity of the topological semimetal nb3site6, *Phys. Rev. B* **107**, 115115 (2023).
- [52] J. P. Perdew, J. A. Chevary, S. H. Vosko, K. A. Jackson, M. R. Pederson, D. J. Singh, and C. Fiolhais, Atoms, molecules, solids, and surfaces: Applications of the generalized gradient approximation for exchange and correlation, *Phys. Rev. B* **46**, 6671 (1992).
- [53] J. P. Perdew, K. Burke, and M. Ernzerhof, Generalized gradient approximation made simple, *Phys. Rev. Lett.* **77**, 3865 (1996).
- [54] G. Kresse and J. Furthmüller, Efficiency of ab-initio total energy calculations for metals and semiconductors using a plane-wave basis set, *Comput. Mater. Sci.* **6**, 15 (1996).
- [55] G. Kresse and J. Furthmüller, Efficient iterative schemes for ab initio total-energy calculations using a plane-wave basis set, *Phys. Rev. B* **54**, 11169 (1996).
- [56] G. Kresse and D. Joubert, From ultrasoft pseudopotentials to the projector augmented-wave method, *Phys. Rev. B* **59**, 1758 (1999).
- [57] L. E. Vorobeve, E. L. Ivchenko, G. E. Pikus, I. I. Farbshtein, V. A. Shalygin, and A. V. Shturbin, Optical activity in tellurium induced by a current, *JETP Lett.* **29**, 485 (1979).
- [58] S. Suzuki, T. Nukariya, Y. Ueda, T. Otsuka, and M. Asada, High current responsivity and wide modulation bandwidth terahertz detector using high-electron-mobility transistor for wireless communication, *Journal of Infrared, Millimeter, and Terahertz Waves* **37**, 658 (2016).
- [59] S. Cakmakyapan, P. K. Lu, A. Navabi, and M. Jarrahi, Gold-patched graphene nano-strips for high-responsivity and ultrafast photodetection from the vis-

- ible to infrared regime, *Light: Science & Applications* **7**, 20 (2018).
- [60] A. K. Geim and I. V. Grigorieva, Van der waals heterostructures, *Nature* **499**, 419 (2013).
- [61] Y. Liu, N. O. Weiss, X. Duan, H. C. Cheng, Y. Huang, and X. Duan, *Van der waals heterostructures and devices* (2016).